Bismuth-polyoxocation coordination networks: controlling nuclearity and dimension-dependent photocatalysis

Mehran Amiri[a], Alice Lulich[a], Nan-Chieh Chiu[a], Samuel Wolff[a,b], Dylan B. Fast,[a,b] William F. Stickle,[c] Kyriakos C. Stylianou[a], and May Nyman[a*]

[a] Department of Chemistry, Oregon State University, Corvallis, OR 97331

[b] Current affiliation; Intel Corporation, Hillsboro. OR 97124

[c] Hewlett-Packard Co., 1000 NE Circle Blvd., Corvallis, Oregon, 97330

*contact author: may.nyman@oregonstate.edu

Keywords: coordination polymers, Bi-MOFs, bismuth oxoclusters, SAXS, photocatalysis

Abstract

Bismuth-oxocluster nodes for metal-organic frameworks (MOFs) and coordination networks/polymers are less prolific than other families featuring zinc, zirconium, titanium, lanthanides, etc. Yet Bi^{3+} is non-toxic, it readily forms polyoxocations, and its oxides are exploited in photocatalysis. This family of compounds provides opportunity in medicinal and energy applications. Here we show that Bi-node nuclearity depends on solvent polarity, leading to a family of Bi_x-sulfonate/carboxylate coordination networks with x=1-38. Larger nuclearity-node networks were obtained from polar and strongly coordinating solvents, and we attribute the solvent ability to stabilize larger species in solution. The strong role of the solvent and the lesser role of the linker in defining node topologies differs from other MOF syntheses, and is due to the Bi^{3+} intrinsic lone pair that leads to weak node-linker interactions. We describe this family by single-crystal X-ray diffraction (eleven structures), obtained in pure forms and high yield. Ditopic linkers include NDS (1,5-naphthalenedisulfonate), DDBS (2,2'-[biphenyl-4,4'-diylchethane-2,1-diyl] dibenzenesulphonate) and NH_2-benzendicarboxylate (BDC). While the BDC and NDS linkers yield more open-framework topologies that resemble those obtained by carboxylate linkers, topologies with DDBS linkers appear to be in-part driven by association between DDBS-molecules. An *in-situ* small-angle X-ray scattering (SAXS) study of Bi_{38}-DDBS revealed stepwise formation, including Bi_{38}-assembly, pre-organization in solution, followed by crystallization, confirming the less important role of the linker. We demonstrated photocatalytic hydrogen (H_2) generation with select members of the synthesized materials without the benefit of a co-catalyst. Band gap determination from X-ray photoelectron spectroscopy (XPS) and UV-vis data suggest the DDBS linker effectively absorbs in the visible range with ligand-to-Bi-node charge transfer. In addition, materials containing more Bi (larger Bi_{38}-nodes or Bi_6 inorganic chains) exhibit strong UV absorption, also contributing to effective photocatalysis by a different mechanism. All tested materials became black with extensive UV-vis exposure, and XPS, transmission electron microscopy, and X-ray scattering of the black Bi_{38}-framework suggests that Bi^0 forms *in-situ*, without phase segregation. This evolution leads to enhanced photocatalytic performance, perhaps due to increased light absorption.

Introduction

Metal-organic frameworks (MOFs) and related coordination polymers (CPs), composed of inorganic oxometal nodes and organic ditopic linkers, are undoubtedly one of the most studied materials families in the 21st century.[1] The major distinguishing characteristic of MOFs is the permanent large pore volume, broadly exploited for gas storage and separations,[2, 3] and this feature is derived from the arrangement of nodes and rigid linkers (topology) and requires robust metal-ligand bonds. Other emerging related families

are polyoxometalates (POM-based). These include 1) so-called POMOFs, in which polyoxometalates (POMs) interact with MOF frameworks via the POM oxygen and framework metal,[4] and 2) supramolecular assemblies consisting of POMs and organic moieties that assemble by non-covalent interactions.[5] Both CPs and MOFs are further innovated and designed for drug delivery,[6] catalysis,[7-10] magnetism,[11] and luminescence.[12] In designing these materials and optimizing emergent properties; the node, the linker, and the pore solvent need to be considered—rapidly creating an overwhelming synthesis and form-function relationship space to explore. While high throughput screening (computational and experimental) has identified and discovered form-function relationsips[13-15] and optimized syntheses,[16, 17] initial discovery of new phases is largely still executed via traditional synthesis and characterization.

In this study, we explore the synthesis and properties of bismuth (III) -based CPs/MOFs with disulfonate linkers. Bismuth-based coordination networks have been far less prolific than transition-metal node MOF families such as group IV (Ti, Zr, and Hf) and Cr, in particular. Challenges include the insolubility of the Bi-precursor and the unavoidable structure-directing effect of the lone pair. On the other hand, bismuth-based materials have unique and useful characteristics, including 1) negligible toxicity (i.e., as a Pb-substitute in materials, or for medicinal applications),[18, 19] 2) indirect bandgap utilized for conductivity and photocatalysis,[20, 21] and 3) high absorption cross-section of extreme UV energy, exploited in nanolithography.[22] The majority of published Bi-oxo MOFs and CPs exploit carboxylate linkers and feature monomer, dimer, trimer, tetramer, and chain building units (**Table S1)**.[23-32]

Bi(III) has known cluster nuclearities ranging from 1 to 38,[33] allowing testing hypotheses about properties related to MOF-node nuclearity and determining reaction pathways to control CP/MOF-node nuclearity. The isolated **Bi_6** cluster, i.e. $[Bi_6O_4(OH)_4(NO_3)_6(H_2O)_2]$ has certainly been a target as a MOF node, given its similar topology to the Zr/Hf_6 node in the well-known UiO-66 MOF.[34, 35] Surprisingly the first **Bi_6** MOF with permanent porosity was only reported in 2019,[30] and Bi_6-CP in 2018.[36] By employing a sulfonatocarboxylate linker, Stock and coworkers created a series of CPs featuring Bi-oxocluster nodes including Bi_6, and even a unique Bi_{16} cluster topology node.[16] Bi_{22} (also an unprecedented oxo-cluster) was isolated in a CP network with a disulfonate linker.[36] We hypothesize that sulfonate linkers behave more as spectators in oxocluster assembly processes and other parameters, such as solvent polarity play a stronger role in dictating cluster nuclearity. Because we are targeting an understanding of (1) how to control oxocluster-node nuclearity and (2) MOF/CP properties as a function of node nuclearity, we exploit disulfonate as a linker for Bi-oxo cluster materials.

Mehring and colleagues showed that **Bi_6** dissolved in DMSO undergoes disassembly-reassembly to form a large cluster with a core composition of $[Bi_{38}O_{45}]$ (Bi_{38}) determined by X-ray scattering; an example complete formula is $[Bi_{38}O_{45}(C_4H_7SO_3)_8(NO_3)_{14}(DMSO)_{19.5}(H_2O)_2]$, determined by single-crystal X-ray diffraction.[33, 37] Bi_{38} is topologically similar to U_{38},[38] Pu_{38},[39, 40] Ce_{38},[41] and Np_{38};[42] and these 1.5 nanometer sized clusters approach metal oxide nanoparticles in diameter and nuclearity. Therefore, Bi_{38} is certainly a targeted node since it is more broadly related to the tetravalent metal-oxo clusters ($Zr/Hf/Ce/Th/U/Np/Pu^{IV}$),[34, 43-47] as well as topologically and compositionally similar metal oxides and viable MOF families. Intriguingly, Bi_{38} was also recently described as a major species in Pepto Bismol[48] via X-ray scattering studies.

Using the **DDBS (**disodium 2,2'-[biphenyl-4,4'-diylchethane-2,1-diyl]dibenzenesulphonate) and **1,5-NDS** (1,5-naphthalene disulfonate) linkers (**figure 1**), Bi nitrate, Bi_2O_3, or pre-formed Bi_6 as a bismuth source, and a variety of solvent/temperature/time parameters; we have identified and attempted to rationalize reaction parameters that control node nuclearity. These efforts have yielded eleven new structures featuring Bi-oxocluster nodes ranging from Bi_1 to Bi_{38} in nuclearity (see **Table 1** and **figure 1).** The Bi_{38}-DDBS and Bi_{38}-NDS represent the largest oxocluster node isolated in a CP/MOF matrix. Second, we used small-angle X-ray scattering (SAXS) with *in-situ* heating to follow the assembly of the Bi_{38}-DDBS

phase, and this sequentially showed 1) assembly of Bi_{38}, 2) pre-organization of the clusters in solution upon adding the linker, and 3) crystallization of the expected phase, plus an additional phase with an even larger unit cell (not yet structurally characterized). The latter represents opportunity to discover new phases, advantaged by the *in-situ* measurements.

We have also demonstrated photocatalytic H_2 production without the benefit of a co-catalyst, and Bi-networks with the DDBS linker and/or higher Bi-content (larger nodes) were most effective. Metal oxides, including Bi oxides have amply demonstrated photocatalytic H_2 production, specifically BiOX (X = Cl, Br, I),[49] Bi_2MO_6 (M = Mo, W),[50] $BiVO_4$,[51] $BiOIO_3$,[52] and Bi_2O_3.[53] MOFs are explicitly designed for H_2 production by utilizing conjugated aromatic linkers that enhance light absorption across the visible spectrum;[54] the charge separation is generally described as ligand to metal charge transfer (LMCT) from the linker to the node. Studies of H_2 production via water splitting for Bi-based MOFs are few,[54-57] also described as ligand to metal-oxo cluster charge transfer, and the conduction band exhibits sufficient potential in the water reduction process ($E^\circ H^+/H_2$ 0.0 eV vs. SHE (standard hydrogen electrode) at pH=0).[54, 55] The same photocatalytic mechanism is defined for Ti-based MOFs (MIL-125).[8] However, much is not known about this process from an atomic level perspective, since Bi does not exhibit readily reversible redox chemistry. Despite the poorly understood reversible redox chemistry of Bi, a recent paper suggests Bi^{3+} isolated within a lacunary polyoxometalate could also perform water oxidation, initiated by $Bi^{3+} \rightarrow Bi^{5+}$ electrochemical oxidation.[58] An intriguing prospective/review[7] provided several insights into the role of the node in effective H_2 production. Specifically related to the current study, the authors suggested nanometric nodes could mimic properties found in quantum dots (i.e., separation enhanced by surface-trapping of electrons or holes) and that infinite chain 'nodes' could enhance charge mobility. Here we show two mechanisms that contribute to effective photocatalysis in Bi-networks; ligand-to-metal charge transfer, and direct light absorption by the Bi-nodes.

Experimental section:

Synthetic details for the twelve reported compounds (eleven Bi-CP/MOFs plus one inorganic Bi-oxysulfate to benchmark photocatalysis of a related inorganic phase) are summarized in the SI and in **Table 1**, discussed below. In addition to single-crystal X-ray diffraction, bulk samples were characterized by powder X-ray diffraction (PXRD, **figures S2-S3)** and UV-vis measurements (**figure S4**). Notably, comparing experimental and calculated PXRD does not show perfect agreement. This is due to two issues. First, preferred orientation is common with acicular clusters, and the observed peak intensities don't necessarily match the calculated peak intensities. Second, the larger node clusters (Bi_{38} in particular) lose some solvent that occupies the voids, which leads to degraded peak intensity and peak definition. Single crystal X-ray diffraction (SCXRD) methods and tables of crystallographic data (**Tables S2-S7**) are summarized in the SI for the reported twelve compounds. These also include representative images of the node and linker in polyhedral representation for identity, and ellipsoid representation of the node (including only Bi, O and S). It was not possible to locate protons for OH groups of the nodes. Rather these are identified by bond valence sum (BVS) calculations, summarized in **Tables S8-S16**. Methods and instrumentation for *in-situ* SAXS studies and photocatalysis studies are also summarized in the SI.

Results and discussion

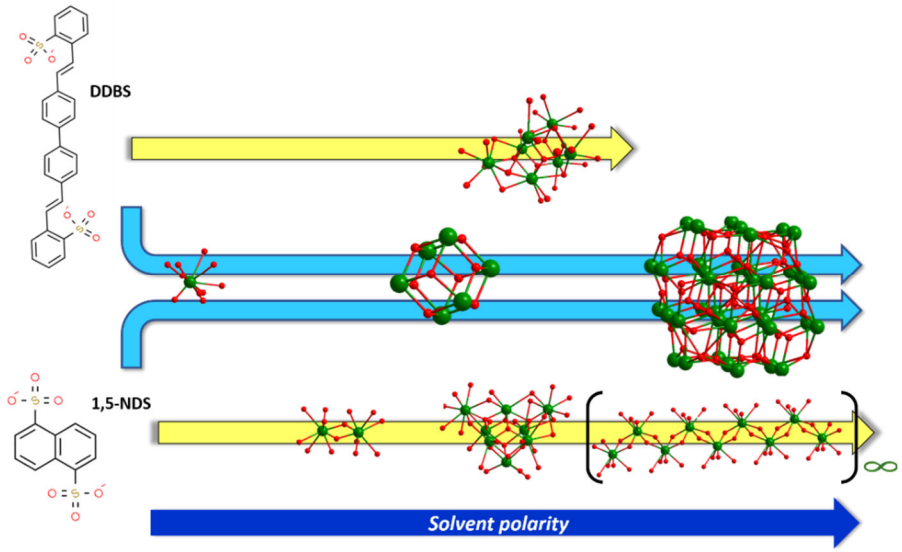

Figure 1. Schematic summary of synthesis results, highlighting the MOF/CP nodes obtained with DDBS (top left) and 1,5-NDS (bottom left) linkers. Green is Bi, red is O. Yellow arrows represent nodes obtained from either DDBS (Bi_7) or NDS (Bi_2, Bi_8, Bi-chains); blue arrows represent nodes obtained from both linker types (Bi_1, Bi_6, Bi_{38}).

Synthesis. The large number of obtained frameworks with node nuclearities ranging from 1 to 38 provides opportunity to consider synthesis parameters that influence node nuclearity, summarized below. **Table 1** and **figure 1** summarize the synthesis conditions and obtained node nuclearity for materials created with both 1,5-NDS and DDBS linkers, and some trends emerge. Following the observation by Mehring and Jensen,[33] we dissolved Bi_6 in DMSO to target the Bi_{38} cluster node. However, to start with a clear solution with the added linker (and to enable SAXS studies), a co-solvent was required. With DMF as the co-solvent and 80 °C reaction temperature, we obtained frameworks containing Bi_{38} with both studied linkers, denoted Bi_{38}-DDBS and Bi_{38}-NDS. For the additional Bi_x-NDS phases, Bi_2O_3 proved to be an effective precursor, while DDBS phases were obtained from $Bi(NO_3)_3$. In every reaction that yielded crystalline phases (other than Bi_{38}-phases), water was a co-solvent, in order to dissolve the linker. In these reactions, the second (and third in some cases) co-solvent differentiated the obtained linker nodes; DMSO gave Bi_6; water yielded Bi-oxo chains; water and methanol Bi_2; and water, DMSO, and acetone Bi_1. The same water-DMSO-acetone mixture with DDBS likewise yielded the monomer. Similarly, H_2O and DMSO plus the respective linker produced Bi_6-phases. The solvent plays a vital role in defining the node nuclearity, but the complex matrix of reactants and solvents challenges a straightforward explanation. However, yields for these reactions are high, and reactions are reproducible without amorphous impurities. The pH for the DDBS solutions (with bismuth nitrate) is ~1.8, whereas the pH for the NDS solutions is approximately 2.0. With Bi_2O_3 as the bismuth source, the low pH is important for retaining the Bi in solution to avoid amorphous precipitates. Considering the smallest nodes, Bi_1, the addition of acetone likely decreases the solvent polarity sufficiently so that only very small bismuth-oxo species can be retained in the solution to form ordered phases. Although water is a very polar solvent, its role in oxocluster assembly also includes driving hydrolysis reactions, which can result in larger nodes, chains, or simply precipitation of oxides. Based on these details, though seemingly counterintuitive, we conclude that more polar and coordinating solvents (i.e., DMSO, DMF) can solubilize and stabilize large Bi-oxo clusters, mainly Bi_6 and Bi_{38}, promoting the formation of frameworks containing these large-node phases. On the other hand, the presence of weakly coordinating solvents such

as acetone, or water that drive hydrolysis/precipitation of oxides (as a competing reaction to linker-node complexation), could only maintain small nodes (i.e. monomers) in solution, leading to crystallization of frameworks that contain smaller nodes. Of the two most polar solvents, DMSO is present in all the reaction solutions (in addition to co-solvents), but only DMF plus DMSO yielded the crystalline frameworks containing Bi_6, Bi_8 and Bi_{38}. This can be compared to a prior reaction pathway study that documented the conversion of clusters, Bi_6 to Bi_{38}, by dissolving the former in DMSO.[33] In their study, in low concentration (DMSO/dichloromethane mass spectrometry experiments), only Bi_6 was observed, whereas higher concentration (DMSO only) X-ray scattering experiments evidenced only Bi_{38}.[33] This suggests Bi_6 and Bi_{38} are similarly favored in polar solvents. The necessity to utilize complex solvent mixtures in our studies arose from the challenges to dissolve both linkers and poorly soluble bismuth precursors; therefore, conclusions regarding control over node nuclearity and dimensionality are not absolute. In addition, while most reactions were carried out at 80 °C, two reported frameworks were grown at room temperature (**Bi_{chain}-NDS** and **Bi_8-NDS-BDC)**, so this is another confounding parameter. Interestingly, Bi_{chain} and Bi_8 frameworks with a fluorinated carboxylate linker were also obtained at room temperature.[59]

We can say more definitively that solvent plays a more important role than linkers in defining bismuth-oxocluster topologies and nuclearity. This is different than the tetravalent metal cations, in which carboxylate ligands and linkers direct the formation of the hexamer cluster[60]/node.[35, 43, 44, 46, 47] This is likely because the Bi^{3+} lone pair inhibits strong bonding between the linker and the node. A clear topology-directing parameter that emerges in the detailed structure descriptions below is the pi-pi stacking of the long, flexible DDBS linkers with each other. The pi-pi stacking is enabled via side-by-side association of DDBS bi-anions, promoting linear connectivity of nodes, rather than 3d connectivity. On the other hand, the shorter and more rigid NDS anions yield more predictable topologies; i.e., resembling structures with carboxylate linkers, including the well-known **scu**-topology.

Table 1. Summary of synthesized compounds and conditions

Node nuclearity	DDBS, brief synthesis description	1,5 NDS, brief synthesis description
Bi_1	$Bi(NO_3)_3$+ DDBS in H_2O + DMSO + acetone (80 °C)	Bi_2O_3+ 1,5 NDS in H_2O + DMSO + acetone (80 °C)
Bi_2		Bi_2O_3+ 1,5 NDS in H_2O + MeOH (80 °C)
Bi_{chain}		Bi_2O_3+ 1,5 NDS in H_2O (80 °C)
Bi_6	$Bi(NO_3)_3$+ DDBS in H_2O+DMSO (80 °C)	Bi_2O_3+ 1,5 NDS in H_2O + DMF (Bi_6-NDS-1) or DMF/H_2O (Bi_6-NDS-2) (2 d, RT)
Bi_7	Double concentration $Bi(NO_3)_3$ concentrated+ DDBS in H_2O+DMSO (80 °C)	
Bi_8		Bi_2O_3+ 1,5 NDS in H_2O + DMSO (80 °C) + 2-amino-BDC in DMF (7 d, RT)
Bi_{38}	Bi_6 cluster in DMSO+ DDBS in DMF (80 °C)	Bi_6 cluster in DMSO+ 1,5-NDS in DMF (80 °C)

Structure Descriptions

Both the DDBS and the 1,5-NDS linker isolated compounds with the monomer, **Bi_1** node. **Bi_1-DDBS** crystallized in the *C*2/*c* space group with a unit cell volume of 11265.8(6) Å^3 (**Table S2**), formulated [Bi(H_2O)(DDBS)$_{1.5}$(DMSO)$_4$ 2H_2O]. Each **Bi_1-**node bridges neighboring nodes via DDBS linkers along the *c*-direction, creating a 1-dimensional material. One DDBS is chelating with Bi-O bond lengths of 2.4 Å and 2.8 Å, and the second is singly-bound with a bond length of 2.6 Å. The Bi coordination sphere is completed with four DMSO ligands with the shortest bond lengths (~2.1-2.2 Å) and one water molecule (Bi-O ~2.5 Å). There is disorder in the Bi-site (85% Bi1A, 15% Bi1B), as well as three of the four DMSO ligands. **Figure 2a** shows an extended unit cell view, down the *b*-axis. An emerging theme with the DDBS linker is interactions between the linkers (i.e., by pi-pi stacking) seems to be a structure directing effect. For **Bi_1-DDBS**, neighboring DDBS molecules are aligned perpendicular (**figure 2b**), with H-H distances of around 2.8 Å, suggesting dispersion forces are involved.

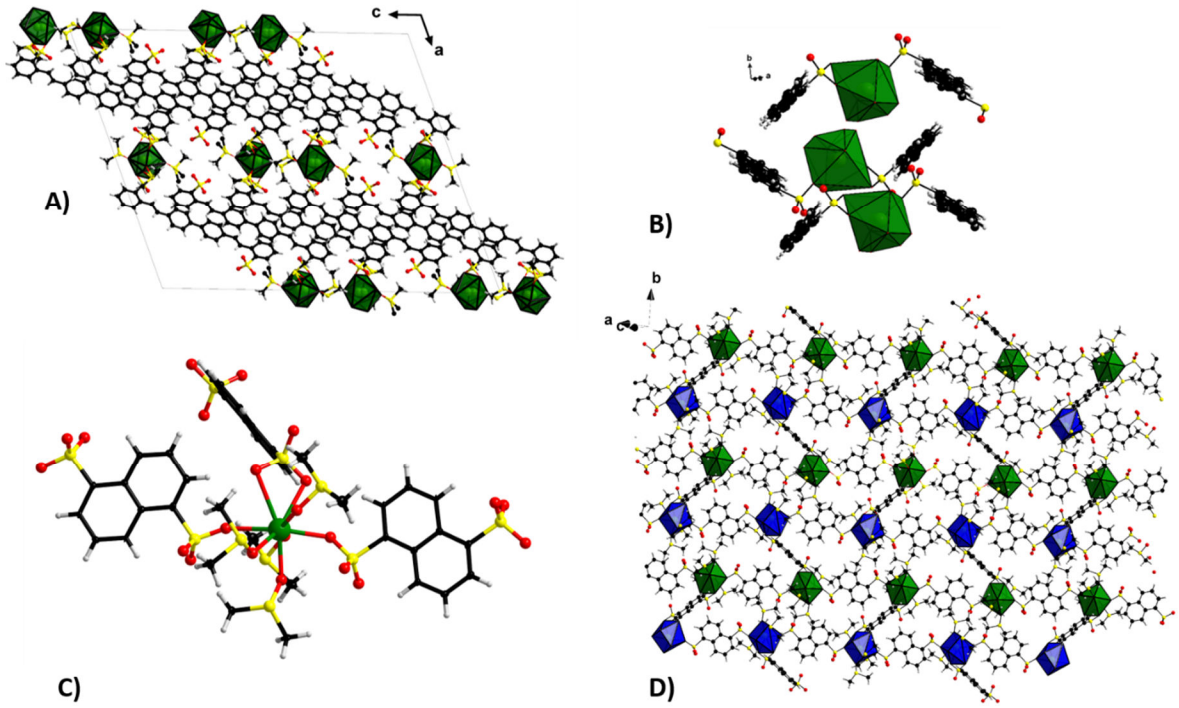

Figure 2. **Views of Bi_1 phases**. **A)** view down the *b*-axis of **Bi_1-DDBS** showing the one-dimensional arrangement. **B)** View of adjacent monomers of **Bi_1-DDBS**, highlighting the perpendicular orientation of neighboring DDBS molecules. **C) Bi_1-NDS** monomer. **D)** View of **Bi_1-NDS** showing the staggered planar arrangement of the layered material. The green and blue (Bi) polyhedra are offset approximately perpendicular to the layer direction, creating a double-decker layer. Atom color codes: green=Bi; red=O; black=C; yellow=S; light gray=H. This color code applies to all structure figures unless stated otherwise.

Bi_1-NDS is a 2-dimensional layered structure, formulated [Bi(1,5-NDS)$_{1.5}$(DMSO)$_4$] and crystallizes in the *P*2$_1$/*c* monoclinic space group with a unit cell volume of 3251.54(4) Å^3 (**Table S2**). The Bi-coordination is highlighted in **figure 2C**, with four bonds to DMSO (Bi-O_{DMSO} ~ 2.3-2.4 Å). The

monomers are linked by three 1,5-NDS ligands. The two monodentate linkers are oriented so the conjugated rings lie parallel to the layers, and the third is bidentate, oriented perpendicular to the planes (Bi-$O_{sulfonate}$ ~ 2.3-2.6 Å). The bidentate linker joins the neighboring Bi-monomer out of the plane, creating 'double-decker' layers. A view of these layers is shown in **figure 2D**. Interactions between layers along the stacking direction appear to be via H-bonding of DMSO molecules; the NDS linkers are not involved in these interactions.

Increasing nuclearity, **Bi_2-NDS** features the dihydroxide-bridged dimer (**figure 3A**) with the moiety formula $[Bi_2(OH)_2(H_2O)_4(1,5\text{-}NDS)_2]$. **$Bi_2$-NDS** crystallizes in the *P*-1 space group with a unit cell volume of 3251.54(4) $Å^3$ (**Table S3**). Bond valence sum (BVS) to identify oxo and hydroxyl ligands are summarized in **Table S8**. The dimer is reinforced with four bridging ligands; two hydroxides (Bi-OH ~2.2 Å) and two 1,5-NDS (Bi-$O_{sulfonate}$ ~ 2.3-2.5 Å). Each Bi is capped with a water molecule (Bi-OH_2 ~2.9 Å) and two additional monodentate sulfonates bridging to neighboring dimers (Bi-$O_{sulfonate}$ ~ 2.3-2.5 Å). The dimers are linked in both the *a*-direction via a single sulfonate (inorganic chains), and the *b*-direction via both sulfonates on opposite sides of the naphthalene, creating alternating layers of linkers and Bi-dimers (**figure 3B**).

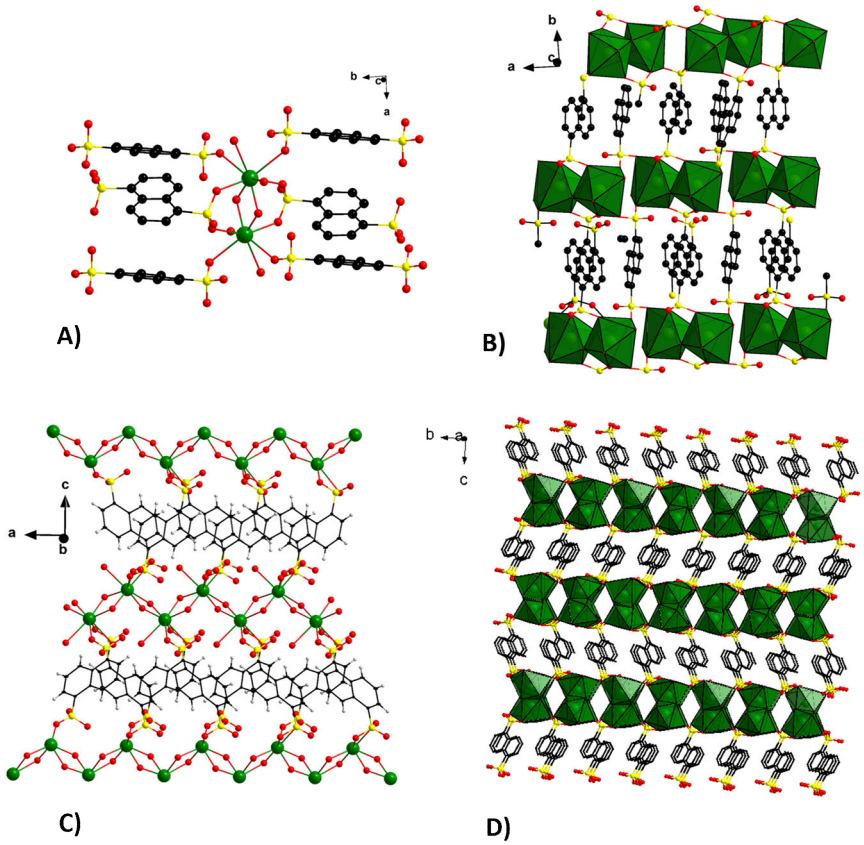

Figure 3. Views of **Bi_2-NDS** and **Bi_{chain}-NDS.** **A)** Ball-and-stick representation of the **Bi_2-NDS** dimer plus its surrounding ligands. **B)** View down the **Bi_2-NDS** *c*-axis highlighting the inorganic dimer chains along the *a*-axis, and linking of the dimers via the NDS in the *b*-direction. **C)** Ball-and-stick representation of **Bi_{chain}-NDS** highlighting the zig-zag chains of dihydroxide-bridged Bi-polyhedra (8-coordinate), that are linked in the c-direction by 1,5-NDS. **D)** A view of the **Bi_{chain}-NDS** framework down the *a*-axis, perpendicular to the zig-zag chains.

The **Bi_{chain}-NDS**, formulated $[Bi_2(OH)_4(H_2O)_2(1,5\text{-NDS})]$ crystallizes in the orthorhombic *P*bca space group with a cell volume of 1600.83(4) $Å^3$ (**Table S3**). This framework features zig-zag chains of edge-sharing (dihydroxide bridged) Bi-polyhedra (8-coordinate) that run along the *a*-axis (**figure 3C-D**). The Bi-OH bond lengths are ~ 2.1-2.4 Å, and each Bi links to four of these. Each Bi is further coordinated to two sulfonate groups, one bidentate and one monodentate with longer bond lengths, ~ 2.8-2.9 Å, and a terminal water molecule with the bond length of 2.6 Å. BVS calculations identifying the protonation of oxo-ligands (i.e., water, hydroxide) are in **Table S9**. The singly bound sulfonate bridges to the neighboring chain in the *b*-direction, which is bidentate-bound to the neighboring chain, thus linking the chains into layers in the *b*-direction. In approximately the *c*-direction, the bidentate sulfonate links to neighboring 'layers', where layers are chains linked by sulfonates within the *ab*-plane (**figure 3D**).

Bi_6-node materials were obtained from both DDBS and the NDS (two different topologies), and these structures are described briefly below. All three structures feature a $Bi_6(OH)_4O_4$ node with disorder of the OH and O over all eight sites, as also typically observed in $M^{IV}(OH)_4O_4$ (M=Zr, Hf, Ce, Pu, Np), i.e. in UiO-66 analogues.[34, 35, 43-47] Likewise, prior-reported Bi_6-MOF[30] and isolated clusters[37, 61] feature the $Bi_6(OH)_4O_4$ ligation. Typical Bi-O bond distances are 2.15-2.19 Å and Bi-O-Bi bond angles are 116-118 °. Typical Bi-OH bond distances are 2.3-2.4 Å and Bi-O(H)-Bi bond angles are 100-102 °. Bi_6-DDBS has an addition complexity of 4 of the 6 Bi of the hexamer are disordered with 0.9/0/1 occupancy, and this is summarized in **Table S10**. The protons were not located on the oxygens in the electron density map, rather BVS (and precedence) informed identity of the hydroxides. (**Tables S10, S12 and S13**).

Bi_6-DDBS crystallizes in the *P*-1 space group with a unit cell volume of 6215.00(16) $Å^3$ (**Table S4**), and it is formulated $[Bi_6(OH)_4O_4(H_2O)_4(DBBS)_3(DMSO)_4{\cdot}2H_2O(DMSO)]$. The **$Bi_6$**-nodes (**figure 4A**) are connected into a 2-dimensional network via six DDBS linkers (**figure 4B** and **4C**). Three DDBS are bridging two Bi-centers within a hexamer, and three are bonded to single Bi in the hexamer, with Bi-O_{DDBS} bond lengths ranging from 2.6 Å to 2.8 Å. Of the six DDBS linkers bonded to a hexamer, four of these link Bi_6-oxoclusters into chains, alternating $[Bi_6\text{-}2DDBS\text{-}Bi_6]_\infty$, and two of them link to neighboring chains (**figure 4C**), based on both charge-balance and BVS (**Table S10**). Per cluster, four of the Bi are capped by a DMSO molecule, and three by an H_2O molecule (bond distances range from 2.5-2.7 Å). The Bi_6 nodes align approximately in the (110) direction and the DDBS-Bi_6 chains run perpendicular. (**figure S4**).

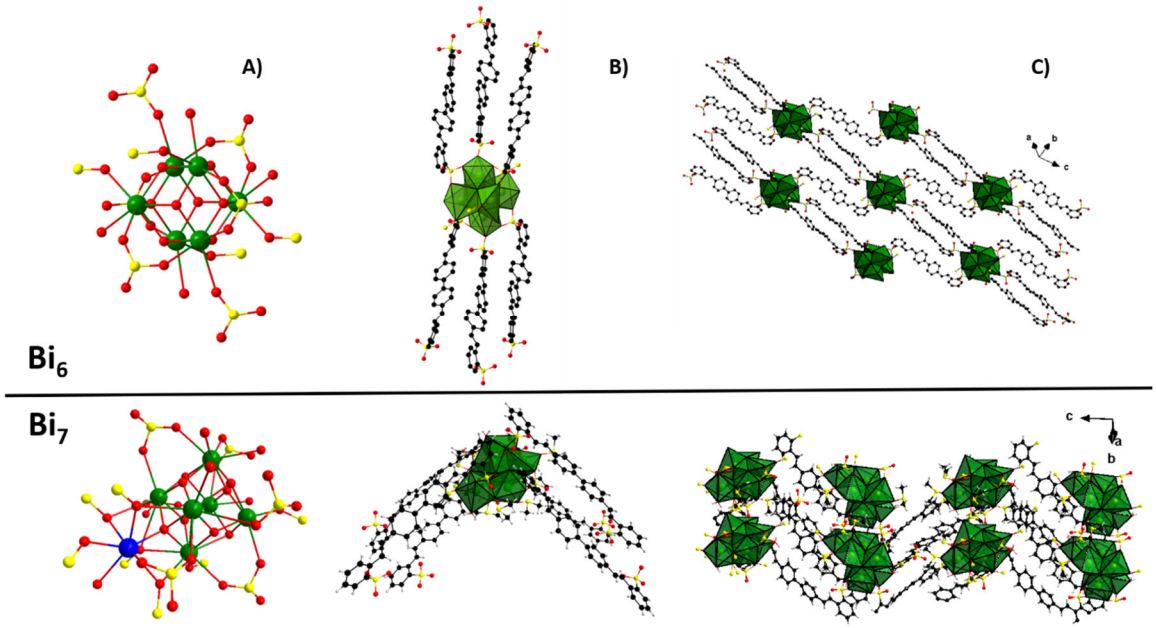

Figure 4. Comparison of **Bi_6-DDBS (top)** and **Bi_7-DDBS (bottom)**. **A)** A single Bi_6-node and Bi_7-node in ball-and-stick representation. Carbons and hydrogens are not shown for ease of viewing. The 'extra' Bi in Bi_7 is highlighted in blue. **B)** View of Bi_6 and Bi_7, each connected to the six DDBS linkers highlighting the difference in linker orientation. **C)** Extended unit cell view highlighting the parallel $[Bi_6\text{-DDBS-}Bi_6]_\infty$ chains and zig-zag $[Bi_7\text{-DDBS-}Bi_7]_\infty$ chains. Green spheres and polyhedra are bismuth, red, black and yellow are respectively oxygen, sulfur and carbon for DMSO.

Synthetically, the only difference between obtaining **Bi_7-DDBS** and the above-described **Bi_6-DDBS** was doubling the Bi nitrate precursor for the former. **Bi_7-DDBS,** formulated $[Bi_7O_5(OH)_3(H_2O)_5(DDBS)_4(DMSO)_7{\cdot}4H_2O]_n$ crystallizes in the $P2_1/c$ monoclinic space group with a unit cell volume of 14830.43(18) Å^3 (**Table S5**). Here we can compare this structure to that of **Bi_6-DDBS** since the node differs by only one polyhedron. The Bi_6-core of Bi_7 has the typical alternating O^{2-} and OH^- of the core hexamer (see BVS, **Table S11**). However, for one OH^- ligand, the proton is replaced by the 7th Bi (**figure 4A**). There are three DDBS sulfonate linkers bridging two Bi-centers; five bridging Bi within the Bi_6-unit and the sixth bridging to the 7th addenda Bi. There are also four DMSO ligands bridging between this 7th Bi and the Bi_6-core, and one terminal DMSO. Within the core Bi_6, there are two additional capping DMSO, and five water ligands. The DDBS Bi-O bond lengths range from 2.5 to 3.2 Å, the DMSO Bi-O 2.5 to 2.8 Å, and Bi-O_{water} 2.7 to 2.9 Å. Whereas the DDBS ligands are aligned in the same direction for Bi_6-DDBS on opposite sides of the cluster, they are aligned at a ~90° angle from opposite sides of the node for Bi_7-DDBS (**figure 4B**), leading to a zig-zag linear arrangement of these chains $[Bi_7\text{-2DDBS-}Bi_7]_\infty$ (**figure 4C**). This Bi_7 cluster has been observed once prior in a Bi-sulfonatocarboxylate framework.[16] Again, the dispersion forces appear to be at play in dictating adjacency of DDBS chains, with H-H distances as short as 2.5 Å.

We obtained two 3-dimensional networks featuring the Bi_6 with 1,5-NDS, formulated $[Bi_6(OH)_4O_4(H_2O)_4(DMF)_2(1,5\text{-NDS})_3]_n$ (**Bi_6-NDS-1**, *P*-1 space group, V=1732.79(4) Å^3) and $[Bi_6(OH)_4O_4(H_2O)_6(DMF)_2(H_{0.5}\text{-}1,5\text{-NDS})_4{\bullet}2H_2O]_n$ (**Bi_6-NDS-2**, tetragonal I4/m, V=4878.06(5) Å^3) (details in **Table S4** for both). The '0.5 H was assigned due to the requirement for an additional 2+ for charge balance. We note there is ambiguity in the oxygen BVS for the S-O-Bi linkages (**Table S13**), so we assume disordered protonation of these linkers. The two frameworks differ in synthesis by the addition of a DMF/water mixture as a co-solvent for **Bi_6-NDS-1**, and pure DMF for **Bi_6-NDS-2**. They only differ in composition by the number of water ligands on the Bi_6-core, but are vastly different in the orientation of the linkers and arrangement of the nodes in the framework (**figure 5A, 6D**). The Bi_6 node of **Bi_6-NDS-1** has six linkers that bridge two metal centers within Bi_6, and two that are singly bound. Bi-$O_{sulfonate}$ bond lengths are ~2.6-2.9 Å. The Bi_6 node of **Bi_6-NDS-2** has all eight linkers bridging two metal centers within Bi_6; Bi-$O_{sulfonate}$ bond lengths are ~2.7 Å. When viewed down the *c*-axis (C_4 axis of the cluster), the eight NDS for **Bi_6-NDS-2** are eclipsed in four sets of two, and each set of two sandwiches a DMF ligand), leading to the tetragonal symmetry. Viewing **Bi_6-NDS-1** down the C_3-axis of the Bi_6-node (**figure 5A**), the symmetry is reduced to an inversion center, by the orientation of the linkers. There are two sets of two eclipsed linkers on opposite sides of the cluster; of each set, one is monodentate, and one is bridging two Bi-centers. The other two sets of bridging linkers are related by inversion centers and are not eclipsed. Interestingly, the four eclipsed NDS of **Bi_6-NDS-1** join the hexamers into entirely inorganic chains along the a-axis (**figure 5C**), via two bridging NDS between Bi_6-units. The remaining four NDS link hexamers into a planar network (**figure 5B**), approximately perpendicular to those joined into chains along the a-axis. **Bi_6-NDS-2** has a much simpler arrangement, resembling the **scu** topology of other M^{IV}_6-MOFS, and the one prior-reported Bi_6-MOF.[30] Each Bi_6 is joined to eight additional Bi_6, in a 3-dimensional network (**figure 5E**).

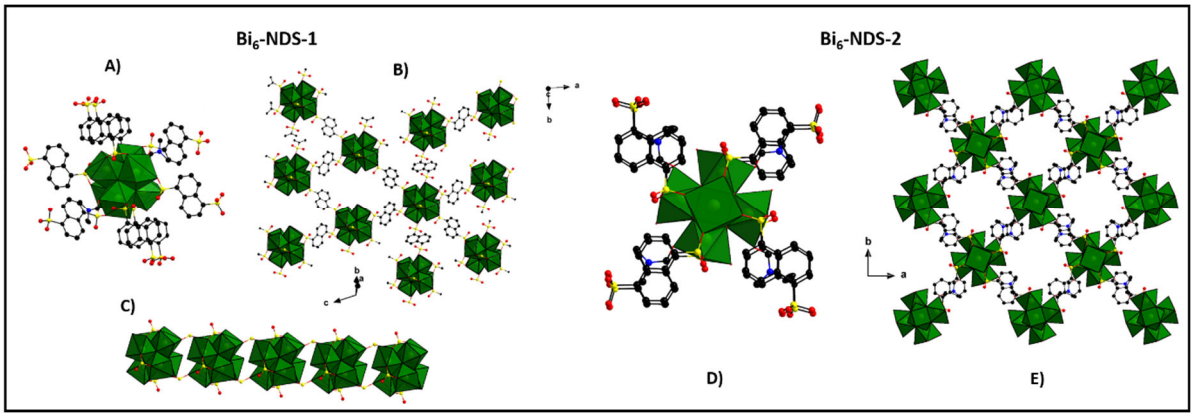

Figure 5. Views of **Bi_6-NDS-1**. **A)** The hexamer plus 8 linking 1,5-NDS. **B)** Planar connectivity of Bi_6, via the non-eclipsed NDS, on the left and right side of the cluster in part A. **C)** Inorganic Bi_6-chains oriented along the *a*-axis and approximately perpendicular to the planar linked clusters shown in part **B**. These are linked by the eclipsed NDS, on the top and bottom of the Bi_6 in part **A**. **D-E.** Views of **Bi_6-NDS-2** with **scu** topology. **D**) A single Bi_6-node highlighting the eight NDS-linkers. **E**) *c*-axis view of the extended 3-dimensional network.

A **Bi_8** cluster node was also obtained in a framework, with a mixture of 1,5-NDS ligands and 2-aminoterephthalic acid (NH_2-BDC), denoted **Bi_8-NDS-BDC** (BDC=benzenedicarboxylate = terephthalic acid). The synthesis is identical to that of the **Bi_6-NDS**, but with the addition of the BDC linker upon cooling the reaction solution. There is clear evidence in the structure that the BDC linker is responsible for the formation of this node**.** **Bi_8-NDS-BDC** is formulated $[Bi_8O_6(OH)_2(1,5NDS)_{2.5}(NH_2BDC)_2(DMSO)_2(DMF)(H_2O)_{4.5}]$ and crystallizes in the triclinic *P*-1 space group, with volume = 6632.56(14) $Å^3$ (**Table S5)**. The basic hexamer core is formulated $Bi_6O_2(OH)_2$ (BVS, **Table S14**) similar to the $Bi_6O_4(OH)_4$, but two hydroxyls are deprotonated because they bridge the two additional Bi-polyhedra, each one linked to three of the core Bi (**figure 6A**). The core is significantly distorted due to the decoration of two additional Bi, with Bi-O bonds within the core ranging from ~2.1-2.6 Å. Each of the decorating Bi is bonded to the core via two NH_2-BDC, so the addition of this ligand is clearly the driving force for the creation of this node. In addition to these four NH_2-BDC linkers per node, there are six 1,5-NDS linkers. Of the NDS linkers, two bridge a decorating Bi and a core Bi, and four bridge two core Bi. Finally, each Bi_8- core has 2 DMSO and 1 DMF ligand. Despite ten linkers extending from each Bi_8 node, each node only links to eight nodes, since two NDS linkers bridge the same two nodes. A view down the *a*-axis reveals an open 3-dimensional structure, resembling a distorted honeycomb (**figure 6B, 6C**) with hexagonal pores parallel to the *a*-axis. The distortion can be observed by the node to node distances. **Figure 6C** is a simplified representation of **Bi_8-NDS-BDC**, and the green spheres represent the Bi_8-node. The center-to-center distances range from 14 to 17 Å, translating the distortion that is observed within the hexamer core to a framework scale.

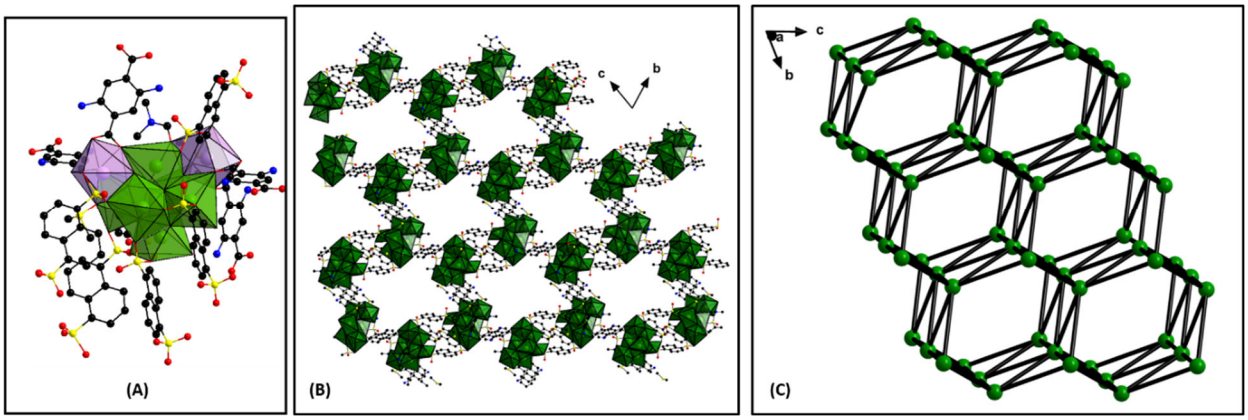

Figure 6. Views of **Bi_8-NDS-BDC. A)** One Bi_8 cluster plus its surrounding linkers and ligands. Blue is N, red is O, black is C, yellow is S. The green polyhedra is the core Bi_6, and the purple are the decorating Bi. **B)** A view down the *a*-axis highlighting the 'honeycomb' framework**. C)** Simplified view of the framework, also approximately viewed down the *a*-axis. The green spheres represent the Bi_8-nodes.

Whereas **Bi_6**-node materials were obtained from DMSO-DMF mixtures starting with Bi_2O_3 or $Bi(NO_3)_3$, when we start with Bi_6-nitrate as the Bi-source dissolved in DMSO, we do indeed obtain materials featuring the Bi_{38}-cluster, as first noted by Mehring and colleagues.[33, 37] We report here frameworks featuring **Bi_{38}** linked by DDBS and by 1,5-NDS. Notably, we have also identified a Bi_{38}-NH_2-BDC (carboxylate) linker framework and a Bi_{38}-2,6-NDS (with **scu** topology) compound via preliminary structures (also obtained with DMSO in the solvent mixture), but these are too low quality to report at the present time. This supports the hypothesis that, unlike the carboxylate linkers, the sulfonate linkers do not play a strong role in directing node topology.

Bi_{38} has been crystallized prior as an isolated cluster, but not in a coordination network with ditopic linkers. **Figure 7A** shows a view of the core cluster without ligands. The central core resembles the Bi_6O_8 building unit that we observe in the hexamer structures, except it has a central μ_6-oxo with six Bi-O bond lengths of 2.55 Å (the six Bi are blue), more similar to the nitrate-ligated Ln(III) hexamers.[62] In considering the central Bi_6 as a cube with Bi occupying the faces of the cube, it is capped with eight Bi (shown in green) on the corners of the cube. This core of 14 Bi is further capped with 24 additional Bi (shown in pink). The 24 Bi can be considered as six squares of four that caps each of the six central Bi. Bi-O distances in the core have a large range from ~2.1 – 3.3 Å, reflecting the lone pair that engenders distorted polyhedra. **Bi_{38}-DDBS** crystallizes in the *P*-1 triclinic space group with a unit cell volume of 9372.8(3) $Å^3$ (**Table S6**), formulated $[Bi_{38}O_{45}(OH)_4(DDBS)_5(NO_3)_{10}(DMSO)_{20}(DMF)_2]$. In **$Bi_{38}$-DDBS (figure 7B),** each Bi_{38}-node is linked to eight DDBS linkers (six bridging the clusters in a linear fashion in the *ab* plane, with Bi-O bond lengths of 2.7 Å to 3 Å (Bi-O distance). Once again, one driving force for assembly seems to be interactions between the DDBS rings, with distances between rings around 3.5 Å. However, the DDBS-DDBS distances are longer in this structure than the above-described structures, and they stack in almost a helical fashion (**see figure S6**). A view down the *b*-axis reveals 2-dimensional connectivity of the **Bi_{38}**-nodes. Each **Bi_{38}** is also capped by twenty DMSO and ten nitrates (NO_3).

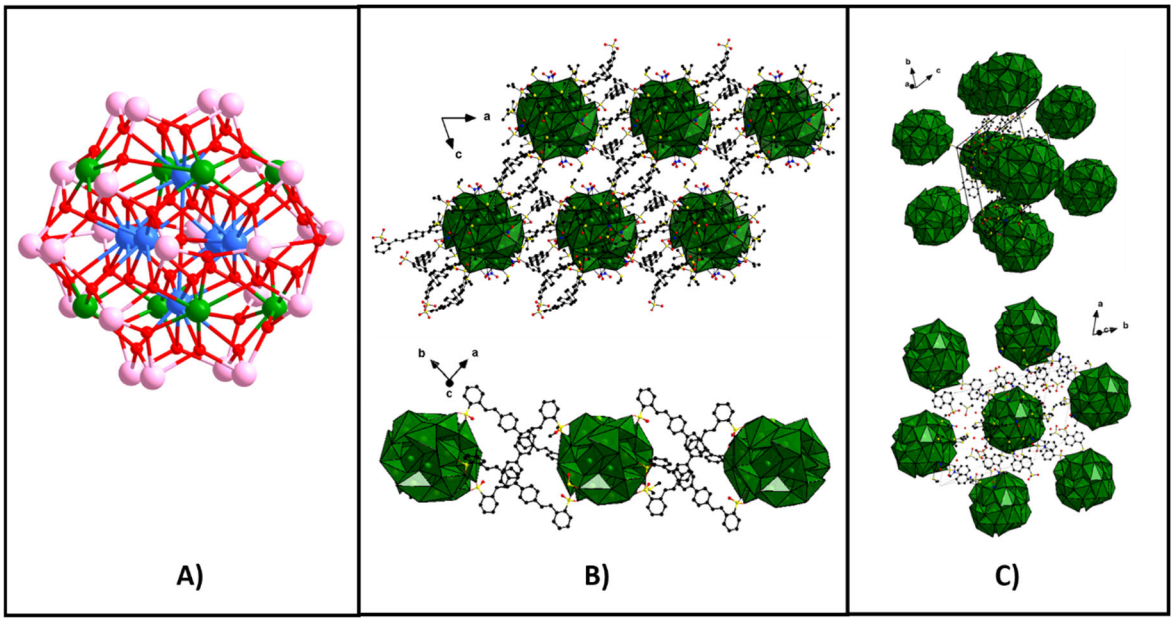

Figure 7. A) View of **Bi_{38}**-node with Bi in blue, green and pink, oxygen in red (see text for explanation). **B)** Views down the *b*-axis (top) and *c*-axis (bottom) of **Bi_{38}-DDBS** highlighting the connectivity of Bi_{38} via the DDBS linkers. **C)** Two views of **Bi_{38}-NDS** highlighting the 3-dimensional arrangement with 10 Bi_{38} surrounding each Bi_{38} (top) and the two-dimensional arrangement resembling a pseudo-closest packed array (bottom).

Bi_{38}-NDS (figure 7C) crystallizes in the triclinic space group *P*-1, with a unit cell volume of 8118.9(2) $Å^3$ (**Table S6,** BVS of oxygens in **Table S15**) and a formula of $[Bi_{38}O_{45}(OH)(1,5\text{-}NDS)_5(NO_3)_{13}(DMSO)_{23}(DMF)_2(H_2O)_2]$. Each Bi_{38} is joined to ten others, via the 1,5-NDS linkers to build a 3-dimensional network. The arrangement on approximately the *ab*-plane resembles a 2-dimensional closest-packed assembly. Normally in a pseudo-closest packing of molecules such as spherical clusters, there are three additional spheres above and below the defined 2-dimensional plane. The arrangement in **Bi_{38}-NDS,** however, involves only two additional linked Bi_{38}, above and below the 2-dimensional plane. The Bi_{38} cluster is bridged by NDS and further capped by DMSO, DMF, water, and nitrate ligands.

*In-situ study of **Bi_{38}-NDS** assembly.* Reported prior and studied by X-ray scattering techniques,[33, 37] Bi_6 dissolved in DMSO undergoes conversion to Bi_{38}. We used SAXS with *in-situ* heating to follow the assembly of **Bi_{38}-DBBS,** albeit with some caveats**.** Specifically, DMSO solvent is highly absorbing, challenging good signal:noise from our lab instrument (see SI for details). In addition, we add the DDBS linker as a DMF solution, so the relative intensities of time points along the reaction pathway cannot be used as part of the data interpretation. Instead, we focus on the Guinier region and prominent structure factor. In the synthesis process, first, we dissolve Bi_6 in DMSO. At room temperature, dissolution takes ~ 5 hours, and the scattering of this solution is the red data points in **figure 8**. The data matches well with that simulated from the Bi_{38} cluster structure (blue line), and the spherical model fit gives a radius of 7.6 Å, similar to that of the simulated scattering for Bi_{38} (**Table 2**).

Upon addition of the DDBS as a DMF solution and initiating heating (see **Table 2**), the primary cluster size remains similar, but a distinct structure factor develops, observed as a broad peak around q=0.25 $Å^{-1}$. Normally a structure factor is observed at higher concentration or in the absence of shielding via counterions. Thus, the observation of this structure factor was initially surprising because we both dilute the Bi_{38}-solution *and* add extra electrolytes upon addition of DDBS. Therefore, the structure factor is due

to the pre-organization of the clusters in solution, prior to the crystallization of **Bi_{38}-DDBS**. The 'eta' parameter, **Table 2**, is half the distance (Å) between the centers of neighboring particles, and the 'phi' parameter is a unitless value that represents the number of nearest neighboring particles. Doubling eta gives center-to-center distance between Bi_{38}, and this is also summarized in **Table 2**. We observe a range of average center-to-center distance, from 28-34 Å, with a general downward trend as the reaction progresses (with heating). The center-to-center distance in **Bi_{38}-DBBS** is 25 Å, and this structure factor provides evidence for the initial assembly in solution, prior to crystallization. In addition, there is an upward swing in the low-q scattering data; particularly at 110-120 ºC, indicating the linear linking of the **Bi_{38}-DDBS** chains that are the primary building unit of these 2-dimensional materials. Finally, we observed diffraction peaks as **Bi_{38}-DBBS** crystallizes in the capillary tube. The higher q (higher angle) peaks are consistent with the **Bi_{38}-DDBS** structure (**figure S7**), and coexist with Bi_{38} scattering, indicating these clusters persist in solution throughout the entire assembly process. Below 2θ=3.5° (**figure S7**), there are additional peaks that represent a crystalline framework (likely also containing Bi_{38}) with an even larger unit cell, that we are yet to isolate and structurally characterize. We suspect it went undetected in the initial ex-situ synthesis and characterization because it was desolvated in the isolation process, diminishing long-range order. This *in-situ* X-ray scattering study highlights the opportunity for new materials discovery by considering reaction pathways. This study also highlights that solvent defines the Bi^{3+}-oxo node instead of the linker.

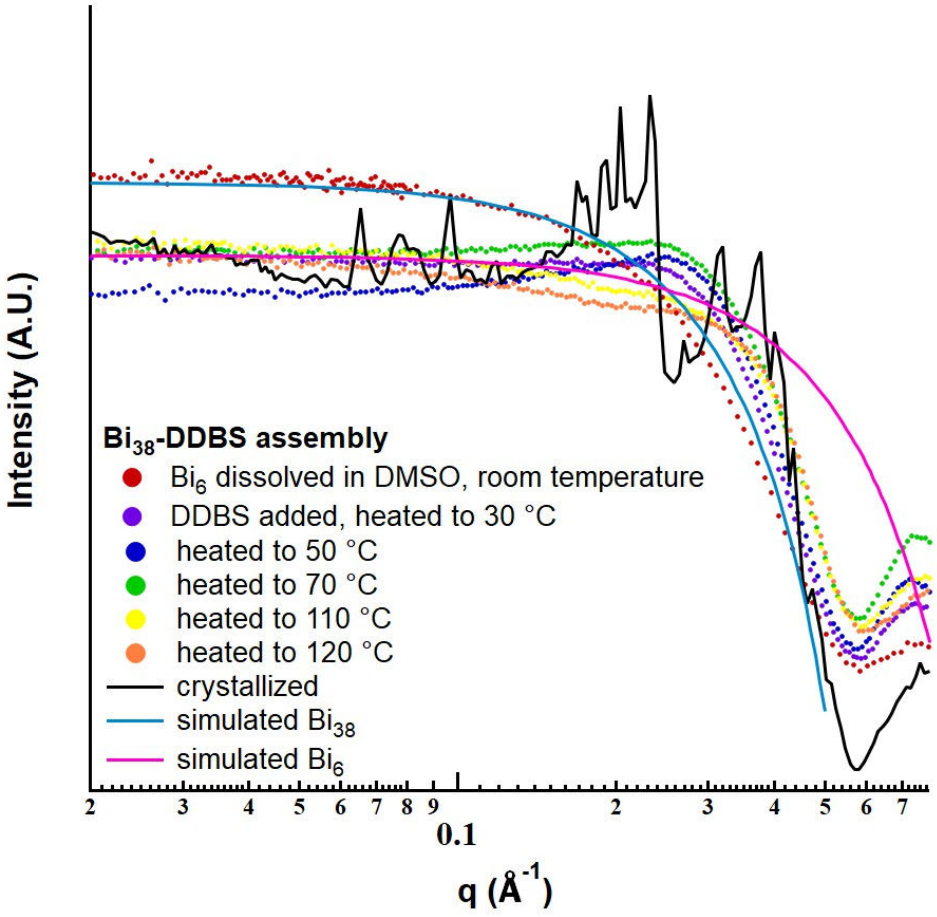

Figure 8. SAXS with *in-situ* heating, benchmarking the solution assembly of Bi_{38}, in-solution linking of DDBS to Bi_{38}, followed by crystallization.

Table 2. Spherical model fitting (with structure factor) of in-situ monitoring of **Bi_{38}-DBBS** assembly

Reaction step	Spherical radius (form factor, Å)	Structure factor[63]		
		Eta (Å)	Center-to-center distance between clusters (Å)	Phi (pack)
Bi_6 dissolved in DMSO, room temperature	7.6	N/A	N/A	N/A
Bi_{38} simulation	7.1	N/A	N/A	N/A
DDBS added, heated to 30 °C	8.1	15	30	1.7
heated to 50 °C	7.2	17	34	2.1
heated to 70 °C	7.5	16	32	1.5
heated to 110 °C	7.4	15	30	4.1
heated to 120 °C	7.3	14	28	4.6

Inorganic $BiOSO_4$ To compare photocatalytically-generated H_2 evolution of the various node-nuclearity coordination networks, we also sought an appropriate inorganic analogue of this family of compounds for comparison. Heating the stock solution for Bi_1-NDS at 175 ºC (described in SI) decomposed the NDS linker and yielded **$BiOSO_4$**, formulated $H_2Bi_2SO_7$ (**Tables S7** and **S16** for crystallographic information and BVS, respectively). The structure has some similarities to BiOX (X=Cl, Br, I), also a demonstrated photocatalyst.[20, 21] Both the BiOX family and **$BiOSO_4$** can be considered a low-dimensional material from the structure-directing effect of the lone pair, with intercalated anions. **$BiOSO_4$** has one-dimensional Bi_2O_3 'ribbons' that run approximately along the *c*-axis. The ribbon is a double row of alternating 3-coordinate and 4-coordinate Bi (Bi-O distances ranging from 2.16 – 2.30 Å, **Table S16**), and these alternate the lone pair pointing on opposite sides of the ribbon, based on the asymmetric coordination environments of these Bi^{3+}. The μ_2- oxygens on the edge of the ribbon are OH^-, and the μ_3- oxygens in the middle of the ribbon are O^{2-} (**figure S8A**). In contrast, BiOX has all 4-coordinate Bi, with similar alternating orientation of the lone pair; but instead of 1d-ribbons, there are 2d-sheets. In **$BiOSO_4$**, the sulfate anions are located between the ribbons, also in rows oriented approximately along the *c*-axis. Similarly, the halides in BiOX are located between the layers. The sulfates have long associations with the lone pair side of the Bi atoms, at ~2.5-2.6 Å. In the ab-plane, the ribbons can be viewed as joined by even longer Bi-O associations, up to 2.9 Å. Considering this 3-dimensional connectivity, **$BiOSO_4$** viewed down the c-axis resembles a dense framework of undulating chains (along the *b*-axis) of connected ribbons, with intercalated sulfate (**figure S8B**). It is up to 4× denser than the related coordination polymers reported here, based on crystallographic information.

Photocatalysis study and related materials characterization

We investigated H_2 evolution via water splitting in this study, using simulated solar radiation. Initially, the Bi compounds were soaked in the reaction media (acetonitrile, water, triethanolamine (TEA) as the sacrificial electron donor), see SI for details, to ensure their stability prior to applying UV-light. PXRD before and after contact with the solution are summarized in **figure S9**. They reveal in some cases changes in peak intensity, but the frameworks are maintained. The energy bandgap (E_g) and valence band and conduction band (VB and CB, respectively) for each Bi-network and cluster were experimentally

calculated through diffuse reflectance and X-ray photoelectron spectroscopy photoelectron spectroscopies (XPS)[64] (**Figures S10-S13**). The CB energy level for all materials is above the energy level of water reduction (H^+/H_2, 0.0 eV vs. NHE (normal hydrogen electrode)), suggesting that they are suitable for reducing water and producing hydrogen (**figure S14, Table S17**). The H_2 (g) evolution rate was evaluated upon irradiation of the Bi-networks, without the use of any co-catalyst to ensure the electron transfer and photoreduction of H_2 are carried out through the Bi-coordination polymer networks. Based on the UV-vis spectra (**figures S4, S10, S11**), **Bi_x-NDS** and Bi-clusters absorb predominantly in the UV-range, whereas **Bi_x-DDBS** absorbs into the visible region of the spectrum. Moreover, the photoluminescence results showed that upon excitation at 355 nm, the Bi_x-DDBS networks emit light with λ_{max} at 450 nm, attributed to ligand to metal charge transfer, while the Bi_x-NDS networks and isolated Bi-clusters do not exhibit this same luminescence (**Figure S15**). **Bi_x-DDBS** structures (x= 1, 6, and 38) were studied to determine the effect of node size (and other parameters) on performance. A comparison of H_2 evolution rate for Bi_{38}-DDBS, Bi_6-DDBS and Bi_1-DDBS is shown in **figure 9A**, and is consistent with higher wt% Bi (or larger nodes) yielded higher H_2 evolution rates. Our highest rates (i.e., Bi_{38}-DDBS and Bi_6-NDS, discussed later) are comparable to that reported earlier by some of us, using UiO-66 derivatives plus a Pt co-catalyst.[65] The Bi_{38} cluster alone did not exhibit H_2 evolution, neither did the DDBS. The bandgaps and respective VB and CB energies for Bi_{38}-DDBS, Bi_6-DDBS and Bi_1-DDBS are all similar (**figure S14, Table S17**), consistent with the photoexcited electrons originating from the DDBS linker, and transferring to the Bi-nodes. The Kubelka-Munk plot (**figure S10**) of the Bi-networks and clusters allows a semi-quantitative comparison of light absorption. Here we can clearly see the absorption contribution of the DDBS (broader band absorption out to 450 nm) and Bi wt% (higher UV absorption), and both are important. The two best photocatalysts tested (**Bi_{38}-DDBS** and **Bi_6-NDS-1, figure 5c,** featuring inorganic chains of **Bi_6)** have comparable absorption intensity in the UV. Surprisingly the absorption of **Bi_6-DDBS** is slightly lower than that of **Bi_1-DDBS**, but that could also be related to the higher ligand content of the latter. Inorganic **$BiOSO_4$** exhibited a lower H_2 evolution rate than **Bi_6-NDS-1** or **Bi_{38}-DDBS**, illustrating the importance of surface area providing access to the nodes, as well as the LMCT mechanism. Based on the above-described results, we can tentatively say that three characteristics contribute to photocatalytic H_2 evolution efficacy: 1) higher Bi-content (larger Bi_{38}-nodes or linked Bi_6-nodes) leading to higher UV-adsorption and/or larger number of catalytic Bi-sites, 2) linkers that absorb into the visible spectrum (DDBS), and 3) porosity for access of the reaction media to the Bi-nodes. An additional consideration in the protonated hydroxyl ligands (i.e. directly-bonded source of H). These are present in the **Bi_6**-node compounds, but not inorganic **$BiOSO_4$** or the **Bi_{38}**-node compounds.

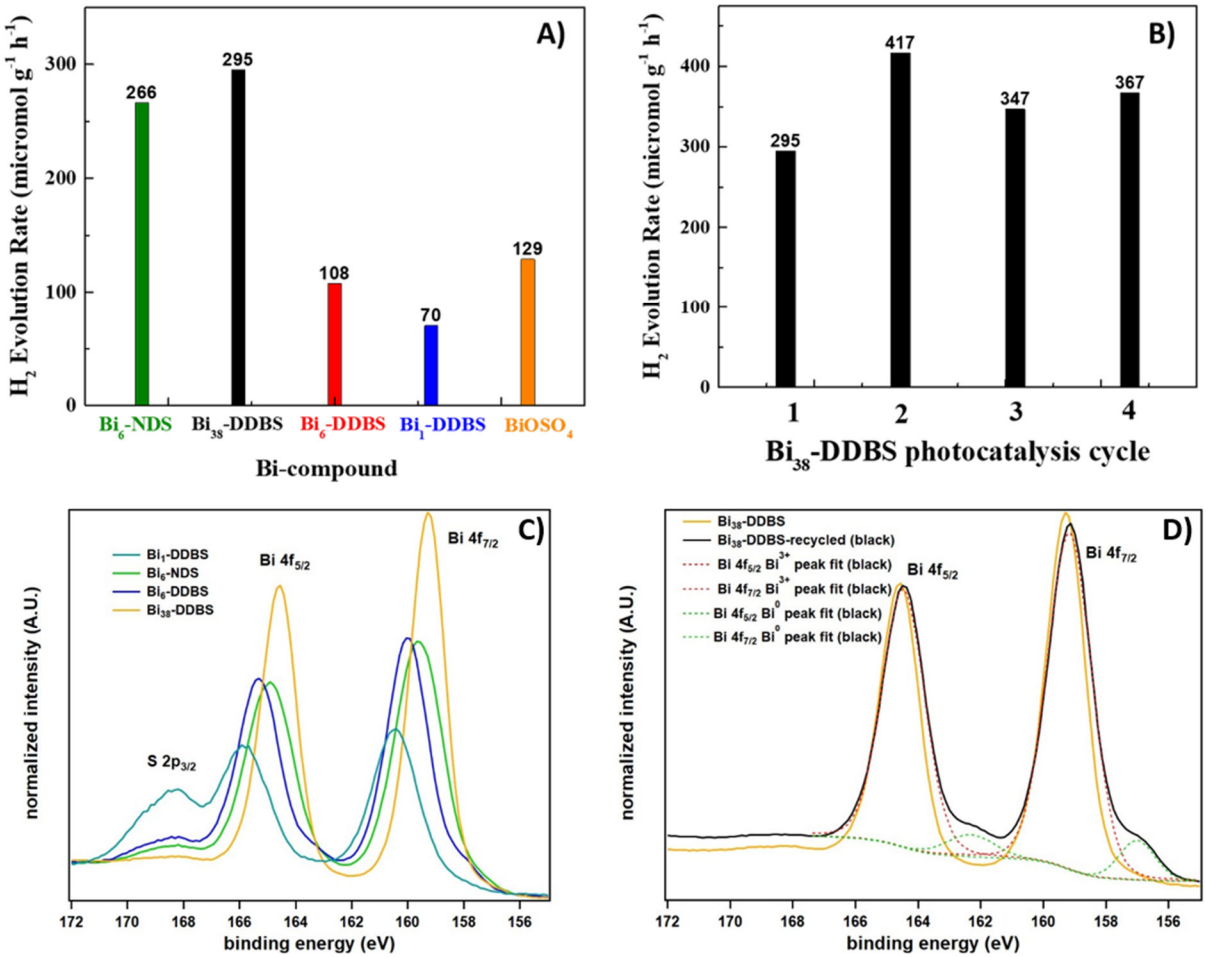

Figure 9. A) H_2 evolution rate of various Bi-compounds under the 300W Arc lamp for 8 hours. B) H_2 evolution of **Bi_{38}-DDBS** for repeated cycles showing increased H_2 evolution rate. C) Bi 4f peaks of Bi photocatalytic materials. D) Bi 4f peaks for Bi_{38}-DDBS fresh, and recycled (black).

With subsequent H_2 evolution cycles of Bi_{38}-DDBS, the H_2 evolution rate increases (**figure 9B**), commensurate with the compound turning black. All of these Bi-containing materials exhibited some degree of color change (white to brown or black), which was reported prior for BiOCl.[66] Enhanced photocatalysis was also noted for BiOCl,[66] and the black color was attributed to oxygen vacancies. However, other factors may be at play, including more effective light absorption across the visible spectrum. The long-range order of Bi_{38}-DDBS (determined by PXRD) post-photocatalysis is diminished, so we characterized Bi_{38}-DDBS before and after the photocatalytic reaction by X-ray total scattering, TEM, and XPS. The pair distribution function (PDF) is shown in **figure S16**, along with the simulated PDF for the Bi_{38}-node. Although this is qualitative data from a lab instrument, we note the major Bi-Bi atom pair scattering is largely-preserved in the 'black' Bi_{38}-DDBS, suggesting preservation of the large Bi_{38} core. TEM analysis confirmed the black color is *not* nanoparticles of elemental bismuth, based on the lack of any diffraction spots or rings (electron diffraction shown in **figure S17).** In prior studies, we have noted that elemental Bi crystallizes readily, even at room temperature and in highly dispersed forms.[67] **Figure 9c** shows the Bi-4f peaks for the studied Bi compounds, and pertinent peak position information is summarized in **Table S18**. All exhibit a single Bi-$4f_{5/2}$ peak (peak positions ranging from 164.4 to165.9 eV) and the $4f_{7/2}$ peak (peak positions ranging from 159.3 to 160.4 eV), with binding energy trending Bi_1<Bi_6<Bi_{38}. By

comparison, Fu reported peak positions for a Bi_6-oxocluster, respectively, at 164.5 and 159.1 eV.[68] To our knowledge, the XPS of Bi_{38} has not been reported. Binding energies for Bi_2O_3 nanoparticles are 158.6 eV and 163.8 eV, respectively, for Bi $4f_{7/2}$ and Bi $4f_{5/2}$.[69] This is most similar to our values for Bi_{38}-DDBS, and consistent with the trend of increasing binding energy with increasing nuclearity. All spectra also exhibit the S $2p_{3/2}$ peak. As expected, the sulfur peak decreases relative intensity with decreasing node size (and decreasing Bi wt%, see **Table S18**).

Figure 9d shows the Bi $4f_{5/2}$ and the $4f_{7/2}$ peaks for Bi_{38}-DDBS, as synthesized, and following photocatalytic cycling (the black material), plus pertinent peak fitting. The Bi-$4f_{5/2}$ and the $4f_{7/2}$ peaks show minimal change in position following photocatalysis, and two new peaks emerge at 162.3 eV and 157.0 eV (8.5% of total bismuth, **Table S18**). These peaks are indeed consistent with Bi^0,[69] similar to that reported prior by Ye for black BiOCl.[66] However, as mentioned above, there is no evidence for phase separation of Bi metal. Therefore, we conclude that the Bi remains dispersed in the black Bi_{38}-DDBS, creating defects in the Bi_{38}-nodes (oxygen vacancies, distortion) that also leads to amorphization of the material. In summarizing the comparative photocatalytic performance of the tested materials, we suggest there are two mechanisms: 1) LMCT of the photoexcited electron, specifically for the Bi_x-DDBS materials, and 2) direct light absorption at the node. Therefore, multiple characteristics emerge that improve efficacy, including: 1) effective visible light absorption of the DDBS and transfer to the Bi-nodes, 2) enhanced light absorption in the black material with prolonged or recycled light exposure, 3) higher Bi-content from larger nodes, enhancing UV absorption (**Table S18**), and 4) open frameworks that allow access to Bi-nodes (i.e., comparing the poorer performance of $BiOSO_4$). Finally, first discovered in 2011[70] but far more extensively studied is black TiO_2, which has some similarities to black Bi photocatalytic materials. In these titania materials, the black color and enhanced photocatalytic activity is attributed to Ti^{3+}, oxygen vacancies, surface disorder, broad spectrum absorption, and a narrowed bandgap.[71] Similar trends may observe from more detailed structural characterization of black bismuth oxides in the future.

Conclusions

Here we have structurally characterized a family of coordination networks/MOFs featuring Bi-oxocluster nodes ranging from monomers to Bi_{38}. To our knowledge, Bi_{38} is the largest inorganic node isolated in such compounds. In addition to the Bi_{38}-DDBS and Bi_{38}-1,5-NDS identified here, we also have preliminary structural data of a several additional Bi_{38} MOFs (with dicarboxylate linkers) that will be reported in due time. Control over node nuclearity was achieved with solvent polarity, where strongly coordinating solvents stabilized larger nodes, regardless of the linker. An *in-situ* SAXS study of Bi_{38}-DDBS evidenced preorganization of the Bi_{38}-clusters in solution upon addition of the linker, prior to any precipitation/crystallization. This affirms that solvent media and not necessarily the linker drives node-nuclearity for Bi-MOFs/CPs, dissimilar to other large node MOF families such as Zr/Hf^{IV}. We attribute this to the intrinsic lone pair of Bi^{3+}, which prohibits strong interaction between the nodes and the linkers. We demonstrated photocatalytic H_2 evolution without the benefit of a co-catalyst. Hydrogen evolution rate increases with increasing node nuclearity (and increasing Bi content) leading to increased light absorption in the UV by the Bi-nodes, as one mechanism. The second mechanism involves LMCT from linker (DDBS) to node. Direct UV absorption of the Bi-nodes led to a black color from photoreduction of Bi^0. Characterization of black Bi_{38}-DDBS showed the Bi^0 does not phase separate and Bi_{38} remains largely intact, and the recycled black material increases H_2 evolution rate. The enhanced photocatalytic activity is attributed to increased light absorption of the black material. In sum, this study demonstrates Bi-MOFs/CPs are promising materials for photocatalytic H_2 evolution, where larger nodes, node interconnectivity, and ligands with visible light absorption all contribute to performance.

Supporting information

The Supporting Information is available free of charge at https://pubs.acs.org/ . Tables of crystallographic information and bond valence sum (BVS) for reported Bi-oxo MOFs and CPs, detailed synthesis and characterization methods (PDF).

Acknowledgements

This study was supported by the U.S. Department of Energy, Office of Basic Energy Sciences, Division of Material Sciences and Engineering, under award DE SC0010802 (MA, AL, MN). KCS and NCC thank the Department of Chemistry at Oregon State University for support through start-up funding (photocatalysis studies). NCC acknowledges support from the Department of Chemistry for the David P. & Clara B. Shoemaker Graduate fellowship. We acknowledge the Murdock Charitable Trust (grant SR-2017297) for acquisition of the single-crystal X-ray diffractometer.

For Table of contents use only

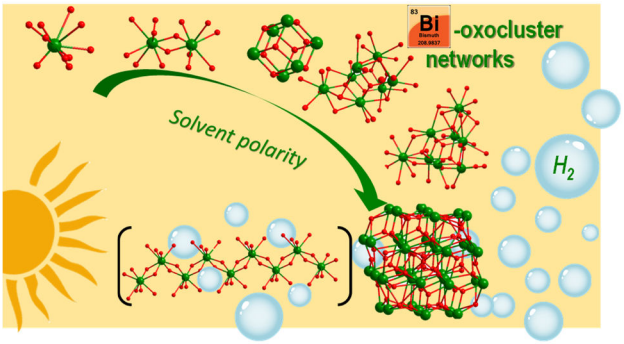

REFERENCES

(1) Maurin, G.; Serre, C.; Cooper, A.; Fereyd, G. The New Age of MOFs and of Their Porous-Related Solids. *Chem Soc Rev* **2017**, *46* (11), 3104-3107. DOI: 10.1039/c7cs90049j.
(2) Altintas, C.; Altundal, O. F.; Keskin, S.; Yildirim, R. Machine Learning Meets with Metal Organic Frameworks for Gas Storage and Separation. *J Chem Inf Model* **2021**, *61* (5), 2131-2146. DOI: 10.1021/acs.jcim.1c00191.
(3) Daglar, H.; Gulbalkan, H. C.; Avci, G.; Aksu, G. O.; Altundal, O. F.; Altintas, C.; Erucar, I.; Keskin, S. Effect of Metal-Organic Framework (MOF) Database Selection on the Assessment of Gas Storage and Separation Potentials of Mofs. *Angew Chem Int Edit* **2021**, *60* (14), 7828-7837. DOI: 10.1002/anie.202015250.
(4) Roy, S.; Vemuri, V.; Maiti, S.; Manoj, K. S.; Subbarao, U.; Peter, S. C. Two Keggin-Based Isostructural POMOF Hybrids: Synthesis, Crystal Structure, and Catalytic Properties. *Inorg Chem* **2018**, *57* (19), 12078-12092. DOI: 10.1021/acs.inorgchem.8b01631.
(5) Roy, S.; Mumbaraddi, D.; Jain, A.; George, S. J.; Peter, S. C. Crystal Engineering in Supramolecular Polyoxometalate Hybrids through pH Controlled in Situ Ligand Hydrolysis. *Inorg Chem* **2018**, *57* (2), 590-601. DOI: 10.1021/acs.inorgchem.7b02385.
(6) Lazaro, I. A.; Forgan, R. S. Application of Zirconium MOFs in Drug Delivery and Biomedicine. *Coordin Chem Rev* **2019**, *380*, 230-259. DOI: 10.1016/j.ccr.2018.09.009.
(7) Dhakshinamoorthy, A.; Asiri, A. M.; Garcia, H. Metal-Organic Framework (MOF) Compounds: Photocatalysts for Redox Reactions and Solar Fuel Production. *Angew Chem Int Edit* **2016**, *55* (18), 5414-5445. DOI: 10.1002/anie.201505581.
(8) Horiuchi, Y.; Toyao, T.; Saito, M.; Mochizuki, K.; Iwata, M.; Higashimura, H.; Anpo, M.; Matsuoka, M. Visible-Light-Promoted Photocatalytic Hydrogen Production by Using an Amino-Functionalized Ti(IV) Metal-Organic Framework. *J Phys Chem C* **2012**, *116* (39), 20848-20853. DOI: 10.1021/jp3046005.
(9) Kampouri, S.; Stylianou, K. C. Dual-Functional Photocatalysis for Simultaneous Hydrogen Production and Oxidation of Organic Substances. *Acs Catal* **2019**, *9* (5), 4247-4270. DOI: 10.1021/acscatal.9b00332.
(10) Yang, H. Z.; Wang, X. Secondary-Component Incorporated Hollow MOFs and Derivatives for Catalytic and Energy-Related Applications. *Adv Mater* **2019**, *31* (38). DOI: ARTN 180074310.1002/adma.201800743.
(11) Espallargas, G. M.; Coronado, E. Magnetic Functionalities in MOFs: From the Framework to the Pore. *Chem Soc Rev* **2018**, *47* (2), 533-557. DOI: 10.1039/c7cs00653e.
(12) Cui, Y. J.; Yue, Y. F.; Qian, G. D.; Chen, B. L. Luminescent Functional Metal-Organic Frameworks. *Chem Rev* **2012**, *112* (2), 1126-1162. DOI: 10.1021/cr200101d.
(13) Altintas, C.; Avci, G.; Daglar, H.; Azar, A. N. V.; Erucar, I.; Velioglu, S.; Keskin, S. An Extensive Comparative Analysis of Two MOF Databases: High-Throughput Screening of Computation-Ready MOFs for CH_4 and H_2 Adsorption. *J Mater Chem A* **2019**, *7* (16), 9593-9608. DOI: 10.1039/c9ta01378d.
(14) Li, S.; Chung, Y. G.; Snurr, R. Q. High-Throughput Screening of Metal-Organic Frameworks for CO_2 Capture in the Presence of Water. *Langmuir* **2016**, *32* (40), 10368-10376. DOI: 10.1021/acs.langmuir.6b02803.
(15) Palomba, J. M.; Harvey, S. P.; Kalaj, M.; Pimentel, B. R.; DeCoste, J. B.; Peterson, G. W.; Cohen, S. M. High-Throughput Screening of MOFs for Breakdown of V-Series Nerve Agents. *Acs Appl Mater Inter* **2020**, *12* (13), 14672-14677. DOI: 10.1021/acsami.9b21693.
(16) Albat, M.; Stock, N. Multiparameter High-Throughput and in Situ X-Ray Diffraction Study of Six New Bismuth Sulfonatocarboxylates: Discovery, Phase Transformation, and Reaction Trends. *Inorg Chem* **2018**, *57* (16), 10352-10363. DOI: 10.1021/acs.inorgchem.8b01563.
(17) Stock, N.; Biswas, S. Synthesis of Metal-Organic Frameworks (MOFs): Routes to Various Mof Topologies, Morphologies, and Composites. *Chem Rev* **2012**, *112* (2), 933-969. DOI: 10.1021/cr200304e.

(18) Miller, N. C.; Bernechea, M. Research Update: Bismuth Based Materials for Photovoltaics. *Apl Mater* **2018**, *6* (8). DOI: Artn 08450310.1063/1.5026541.
(19) Slavney, A. H.; Hu, T.; Lindenberg, A. M.; Karunadasa, H. I. A Bismuth-Halide Double Perovskite with Long Carrier Recombination Lifetime for Photovoltaic Applications. *J Am Chem Soc* **2016**, *138* (7), 2138-2141. DOI: 10.1021/jacs.5b13294.
(20) Jin, X. L.; Ye, L. Q.; Xie, H. Q.; Chen, G. Bismuth-Rich Bismuth Oxyhalides for Environmental and Energy Photocatalysis. *Coordin Chem Rev* **2017**, *349*, 84-101. DOI: 10.1016/j.ccr.2017.08.010.
(21) Li, J.; Yu, Y.; Zhang, L. Z. Bismuth Oxyhalide Nanomaterials: Layered Structures Meet Photocatalysis. *Nanoscale* **2014**, *6* (15), 8473-8488. DOI: 10.1039/c4nr02553a.
(22) Passarelli, J.; Sortland, M.; Del Re, R.; Cardineau, B.; Sarma, C.; Freedman, D. A.; Brainard, R. L. Bismuth Resists for Euv Lithography. *J Photopolym Sci Tec* **2014**, *27* (5), 655-661. DOI: DOI 10.2494/photopolymer.27.655.
(23) Feyand, M.; Koppen, M.; Friedrichs, G.; Stock, N. Bismuth Tri- and Tetraarylcarboxylates: Crystal Structures, in Situ X-Ray Diffraction, Intermediates and Luminescence. *Chem-Eur J* **2013**, *19* (37), 12537-12546. DOI: 10.1002/chem.201301139.
(24) Feyand, M.; Mugnaioli, E.; Vermoortele, F.; Bueken, B.; Dieterich, J. M.; Reimer, T.; Kolb, U.; de Vos, D.; Stock, N. Automated Diffraction Tomography for the Structure Elucidation of Twinned, Sub-Micrometer Crystals of a Highly Porous, Catalytically Active Bismuth Metal-Organic Framework. *Angew Chem Int Edit* **2012**, *51* (41), 10373-10376. DOI: 10.1002/anie.201204963.
(25) Grape, E. S.; Flores, J. G.; Hidalgo, T.; Martinez-Ahumada, E.; Gutierrez-Alejandre, A.; Hautier, A.; Williams, D. R.; O'Keeffe, M.; Ohrstrom, L.; Willhammar, T.; et al. A Robust and Biocompatible Bismuth Ellagate MOF Synthesized under Green Ambient Conditions. *J Am Chem Soc* **2020**, *142* (39), 16795-16804. DOI: 10.1021/jacs.0c07525.
(26) Inge, A. K.; Koppen, M.; Su, J.; Feyand, M.; Xu, H. Y.; Zou, X. D.; O'Keeffe, M.; Stock, N. Unprecedented Topological Complexity in a Metal-Organic Framework Constructed from Simple Building Units. *J Am Chem Soc* **2016**, *138* (6), 1970-1976. DOI: 10.1021/jacs.5b12484.
(27) Koppen, M.; Beyer, O.; Wuttke, S.; Luning, U.; Stock, N. Synthesis, Functionalisation and Post-Synthetic Modification of Bismuth Metal-Organic Frameworks. *Dalton Trans* **2017**, *46* (26), 8658-8663. DOI: 10.1039/c7dt01744h.
(28) Koppen, M.; Meyer, V.; Angstrom, J.; Inge, A. K.; Stock, N. Solvent-Dependent Formation of Three New Bi-Metal-Organic Frameworks Using a Tetracarboxylic Acid. *Cryst Growth Des* **2018**, *18* (7), 4060-4067. DOI: 10.1021/acs.cgd.8b00439.
(29) Orellana-Tavra, C.; Koppen, M.; Li, A.; Stock, N.; Fairen-Jimenez, D. Biocompatible, Crystalline, and Amorphous Bismuth-Based Metal-Organic Frameworks for Drug Delivery. *Acs Appl Mater Inter* **2020**, *12* (5), 5633-5641. DOI: 10.1021/acsami.9b21692.
(30) Robison, L.; Zhang, L.; Drout, R. J.; Li, P.; Haney, C. R.; Brikha, A.; Noh, H.; Mehdi, B. L.; Browning, N. D.; Dravid, V. P.; et al. A Bismuth Metal-Organic Framework as a Contrast Agent for X-Ray Computed Tomography. *Acs Appl Bio Mater* **2019**, *2* (3), 1197-1203. DOI: 10.1021/acsabm.8b00778.
(31) Savage, M.; Yang, S. H.; Suyetin, M.; Bichoutskaia, E.; Lewis, W.; Blake, A. J.; Barnett, S. A.; Schroder, M. A Novel Bismuth-Based Metal-Organic Framework for High Volumetric Methane and Carbon Dioxide Adsorption. *Chem-Eur J* **2014**, *20* (26), 8024-8029. DOI: 10.1002/chem.201304799.
(32) Yuan, W. W.; Wu, J. X.; Zhang, X. D.; Hou, S. Z.; Xu, M.; Gu, Z. Y. In Situ Transformation of Bismuth Metal-Organic Frameworks for Efficient Selective Electroreduction of CO_2 to Formate. *J Mater Chem A* **2020**, *8* (46), 24486-24492. DOI: 10.1039/d0ta08092f.
(33) Anker, A. S.; Christiansen, T. L.; Weber, M.; Schmiele, M.; Brok, E.; Kjaer, E. T. S.; Juhas, P.; Thomas, R.; Mehring, M.; Jensen, K. M. O. Structural Changes During the Growth of Atomically Precise Metal Oxido Nanoclusters from Combined Pair Distribution Function and Small-Angle X-Ray Scattering Analysis. *Angew Chem Int Edit* **2021**, *60* (37), 20407-20416. DOI: 10.1002/anie.202103641.

(34) Cavka, J. H.; Jakobsen, S.; Olsbye, U.; Guillou, N.; Lamberti, C.; Bordiga, S.; Lillerud, K. P. A New Zirconium Inorganic Building Brick Forming Metal Organic Frameworks with Exceptional Stability. *J Am Chem Soc* **2008**, *130* (42), 13850-13851. DOI: 10.1021/ja8057953.
(35) Jakobsen, S.; Gianolio, D.; Wragg, D. S.; Nilsen, M. H.; Emerich, H.; Bordiga, S.; Lamberti, C.; Olsbye, U.; Tilset, M.; Lillerud, K. P. Structural Determination of a Highly Stable Metal-Organic Framework with Possible Application to Interim Radioactive Waste Scavenging: Hf-Uio-66. *Phys Rev B* **2012**, *86* (12). DOI: ARTN 12542910.1103/PhysRevB.86.125429.
(36) Senevirathna, D. C.; Werrett, M. V.; Blair, V. L.; Mehring, M.; Andrews, P. C. 2d and 3d Coordination Networks of Polynuclear Bismuth Oxido/Hydroxido Sulfonato Clusters from Low Temperature Solid-State Metathesis Reactions. *Chem-Eur J* **2018**, *24* (26), 6722-6726. DOI: 10.1002/chem.201705981.
(37) Miersch, L.; Ruffer, T.; Schlesinger, M.; Lang, H.; Mehring, M. Hydrolysis Studies on Bismuth Nitrate: Synthesis and Crystallization of Four Novel Polynuclear Basic Bismuth Nitrates. *Inorg Chem* **2012**, *51* (17), 9376-9384. DOI: 10.1021/ic301148p.
(38) Falaise, C.; Volkringer, C.; Vigier, J. F.; Beaurain, A.; Roussel, P.; Rabu, P.; Loiseau, T. Isolation of the Large {Actinide}(38) Poly-Oxo Cluster with Uranium. *J Am Chem Soc* **2013**, *135* (42), 15678-15681. DOI: 10.1021/ja4067207.
(39) Soderholm, L.; Almond, P. M.; Skanthakumar, S.; Wilson, R. E.; Burns, P. C. The Structure of the Plutonium Oxide Nanocluster $[Pu_{38}O_{56}Cl_{54}(H2O)_8]^{14-}$. *Angew Chem Int Edit* **2008**, *47* (2), 298-302. DOI: 10.1002/anie.200704420.
(40) Wilson, R. E.; Skanthakumar, S.; Soderholm, L. Separation of Plutonium Oxide Nanoparticles and Colloids. *Angew Chem Int Edit* **2011**, *50* (47), 11234-11237. DOI: 10.1002/anie.201105624.
(41) Wasson, M. C.; Zhang, X.; Otake, K. I.; Rosen, A. S.; Alayoglu, S.; Krzyaniak, M. D.; Chen, Z. J.; Redfern, L. R.; Robison, L.; Son, F. A.; et al. Supramolecular Porous Assemblies of Atomically Precise Catalytically Active Cerium-Based Clusters. *Chem Mater* **2020**, *32* (19), 8522-8529. DOI: 10.1021/acs.chemmater.0c02740.
(42) Martin, N. P.; Volkringer, C.; Roussel, P.; Marz, J.; Hennig, C.; Loiseau, T.; Ikeda-Ohno, A. {Np-38} Clusters: The Missing Link in the Largest Poly-Oxo Cluster Series of Tetravalent Actinides. *Chem Commun* **2018**, *54* (72), 10060-10063. DOI: 10.1039/c8cc03744b.
(43) Hastings, A. M.; Ray, D.; Jeong, W.; Gagliardi, L.; Farha, O. K.; Hixon, A. E. Advancement of Actinide Metal-Organic Framework Chemistry Via Synthesis of Pu-Uio-66. *J Am Chem Soc* **2020**, *142* (20), 9363-9371. DOI: 10.1021/jacs.0c01895.
(44) Falaise, C.; Volkringer, C.; Vigier, J. F.; Henry, N.; Beaurain, A.; Loiseau, T. Three-Dimensional Mof-Type Architectures with Tetravalent Uranium Hexanuclear Motifs (U_6O_8). *Chem-Eur J* **2013**, *19* (17), 5324-5331. DOI: 10.1002/chem.201203914.
(45) Martin, N. P.; Marz, J.; Feuchter, H.; Duval, S.; Roussel, P.; Henry, N.; Ikeda-Ohno, A.; Loiseau, T.; Volkringer, C. Synthesis and Structural Characterization of the First Neptunium Based Metal-Organic Frameworks Incorporating $\{Np_6O_8\}$ Hexanuclear Clusters. *Chem Commun* **2018**, *54* (51), 6979-6982. DOI: 10.1039/c8cc03121e.
(46) Lammert, M.; Wharmby, M. T.; Smolders, S.; Bueken, B.; Lieb, A.; Lomachenko, K. A.; De Vos, D.; Stock, N. Cerium-Based Metal Organic Frameworks with Uio-66 Architecture: Synthesis, Properties and Redox Catalytic Activity. *Chem Commun* **2015**, *51* (63), 12578-12581. DOI: 10.1039/c5cc02606g.
(47) Falaise, C.; Charles, J. S.; Volkringer, C.; Loiseau, T. Thorium Terephthalates Coordination Polymers Synthesized in Solvothermal Dmf/H2o System. *Inorg Chem* **2015**, *54* (5), 2235-2242. DOI: 10.1021/ic502725y.
(48) Szczerba, D.; Tan, D.; Do, J. L.; Titi, H. M.; Mouhtadi, S.; Chaumont, D.; de Lucas, M. D. M.; Geoffroy, N.; Meyer, M.; Rousselin, Y.; et al. Real-Time Observation of "Soft" Magic-Size Clusters During Hydrolysis of the Model Metallodrug Bismuth Disalicylate. *J Am Chem Soc* **2021**, *143* (40), 16332-16336. DOI: 10.1021/jacs.1c07186.

(49) Guan, Y.; Wu, J.; Man, X. K.; Liu, Q. Z.; Qi, Y. F.; He, P.; Qi, X. M. Rational Fabrication of Flower-Like $BiOI_{1-X}$ Photocatalyst by Modulating Efficient Iodine Vacancies for Mercury Removal and Dft Study. *Chem Eng J* **2020**, *396*. DOI: ARTN 12523410.1016/j.cej.2020.125234.
(50) Lai, K. R.; Wei, W.; Zhu, Y. T.; Guo, M.; Dai, Y.; Huang, B. B. Effects of Oxygen Vacancy and N-Doping on the Electronic and Photocatalytic Properties of Bi2mo6 (M=Mo, W). *J Solid State Chem* **2012**, *187*, 103-108. DOI: 10.1016/j.jssc.2012.01.004.
(51) Wu, H.; Irani, R.; Zhang, K. F.; Jing, L.; Dai, H. X.; Chung, H. Y.; Abdi, F. F.; Ng, Y. H. Unveiling Carrier Dynamics in Periodic Porous $BiVO_4$ Photocatalyst for Enhanced Solar Water Splitting. *Acs Energy Lett* **2021**, *6* (10), 3400-3407. DOI: 10.1021/acsenergylett.1c01454.
(52) Ji, Z.; Wu, J.; Tian, F. G.; Liu, Q. Z.; Zhao, L. L.; Qu, C. H.; Li, F. Q.; Qi, X. M.; Guan, Y.; Zhang, Y. J. Fabrication of Carbon-Modified $BiOI/BiOIO_3$ Heterostructures with Oxygen Vacancies for Enhancing Photocatalytic Activity. *Catal Lett* **2018**, *148* (11), 3349-3362. DOI: 10.1007/s10562-018-2558-2.
(53) Khalid, N. R.; Israr, Z.; Tahir, M. B.; Iqbal, T. Highly Efficient Bi_2O_3/MoS_2 P-N Heterojunction Photocatalyst for H_2 Evolution from Water Splitting. *Int J Hydrogen Energ* **2020**, *45* (15), 8479-8489. DOI: 10.1016/j.ijhydene.2020.01.031.
(54) Garcia-Sanchez, A.; Gomez-Mendoza, M.; Barawi, M.; Villar-Garcia, I. J.; Liras, M.; Gandara, F.; O'Shea, V. A. D. Fundamental Insights into Photoelectrocatalytic Hydrogen Production with a Hole-Transport Bismuth Metal-Organic Framework. *J Am Chem Soc* **2020**, *142* (1), 318-326. DOI: 10.1021/jacs.9b10261.
(55) Xiao, Y. J.; Guo, X. Y.; Liu, J. X.; Liu, L. F.; Zhang, F. X.; Li, C. Development of a Bismuth-Based Metal-Organic Framework for Photocatalytic Hydrogen Production. *Chinese J Catal* **2019**, *40* (9), 1339-1344. DOI: Doi 10.1016/S1872-2067(19)63329-2.
(56) Wang, G. Z.; Liu, Y. Y.; Huang, B. B.; Qin, X. Y.; Zhang, X. Y.; Dai, Y. A Novel Metal-Organic Framework Based on Bismuth and Trimesic Acid: Synthesis, Structure and Properties. *Dalton Trans* **2015**, *44* (37), 16238-16241. DOI: 10.1039/c5dt03111g.
(57) Wang, G. Z.; Sun, Q. L.; Liu, Y. Y.; Huang, B. B.; Dai, Y.; Zhang, X. Y.; Qin, X. Y. A Bismuth-Based Metal-Organic Framework as an Efficient Visible-Light-Driven Photocatalyst. *Chem-Eur J* **2015**, *21* (6), 2364-2367. DOI: 10.1002/chem.201405047.
(58) Mulkapuri, S.; Ravi, A.; Das, S. K. Fabricating a Functionalized Polyoxometalate with Zif-8: Acomposite Material for Water Oxidation in a Wide Ph Range. *Chem Mater* **2022**, *34* (8), 3624-3636. DOI: 10.1021/acs.chemmater.1c03917.
(59) Lulich, A.; Amiri, M.; Stephen, D.; Shohel, M.; Mao, Z.; Nyman, M. Bismuth Coordination Polymers with Fluorinated Linkers: Aqueous Stability, Bi-Volatility, and Adsorptive Behavior. *ACS Omega* **2023**, published March 6, ASAP. DOI: 10.1021/acsomega.3c00114.
(60) Hennig, C.; Weiss, S.; Kraus, W.; Kretzschmar, J.; Scheinost, A. C. Solution Species and Crystal Structure of Zr(IV) Acetate. *Inorg Chem* **2017**, *56* (5), 2473-2480. DOI: 10.1021/acs.inorgchem.6b01624.
(61) Fernandez, I. I. L.; Donaldson, S. L.; Schipper, D. E.; Andleeb, S.; Whitmire, K. H. Anionic Bismuth-Oxido Carboxylate Clusters with Transition Metal Countercations. *Inorg Chem* **2016**, *55* (21), 11560-11569. DOI: 10.1021/acs.inorgchem.6b02092.
(62) Zak, Z.; Unfried, P.; Giester, G. The Structures of Some Rare-Earth Basic Nitrates $[Ln_6(\mu\text{-}6\text{-}O)(\mu\text{-}3\text{-}OH)_8(H_2O)_{12}(NO_3)_6](NO_3)_2{\cdot}XH_2O$, Ln=Y, Gd, Yb, X(Y, Yb)=4 X(Gd)=5 - a Novel Rare-Earth-Metal Cluster of the M_6X_8 Type with Interstitial O-Atom. *J Alloy Compd* **1994**, *205* (1-2), 235-242. DOI: Doi 10.1016/0925-8388(94)90795-1.
(63) Ilavsky, J.; Jemian, P. R. Irena: Tool Suite for Modeling and Analysis of Small-Angle Scattering. *J Appl Crystallogr* **2009**, *42*, 347-353. DOI: 10.1107/S0021889809002222.
(64) Makula, P.; Pacia, M.; Macyk, W. How to Correctly Determine the Band Gap Energy of Modified Semiconductor Photocatalysts Based on Uv-Vis Spectra. *J Phys Chem Lett* **2018**, *9* (23), 6814-6817. DOI: 10.1021/acs.jpclett.8b02892.

(65) Chiu, N. C.; Nord, M. T.; Tang, L. T.; Lancaster, L. S.; Hirschi, J. S.; Wolff, S. K.; Hutchinson, E. M.; Goulas, K. A.; Stickle, W. F.; Zuehlsdorff, T. J.; et al. Designing Dual-Functional Metal-Organic Frameworks for Photocatalysis. *Chem Mater* **2022**, *34* (19), 8798-8807. DOI: 10.1021/acs.chemmater.2c02089.
(66) Ye, L. Q.; Deng, K. J.; Xu, F.; Tian, L. H.; Peng, T. Y.; Zan, L. Increasing Visible-Light Absorption for Photocatalysis with Black Biocl. *Phys Chem Chem Phys* **2012**, *14* (1), 82-85. DOI: 10.1039/c1cp22876e.
(67) Sadeghi, O.; Falaise, C.; Molina, P. I.; Hufschmid, R.; Campana, C. F.; Noll, B. C.; Browning, N. D.; Nyman, M. Chemical Stabilization and Electrochemical Destabilization of the Iron Keggin Ion in Water. *Inorg Chem* **2016**, *55* (21), 11078-11088. DOI: 10.1021/acs.inorgchem.6b01694.
(68) Fu, M. Y.; Wang, H. Y.; Zhai, H. L.; Zhu, Q. Y.; Dai, J. Assembly of a Titanium-Oxo Cluster and a Bismuth Iodide Cluster, a Single-Source Precursor of a P-N-Type Photocatalyst. *Inorg Chem* **2021**, *60* (13), 9589-9597. DOI: 10.1021/acs.inorgchem.1c00816.
(69) Hwang, G. H.; Han, W. K.; Kim, S. J.; Hong, S. J.; Park, J. S.; Park, H. J.; Kang, S. G. An Electrochemical Preparation of Bismuth Nanoparticles by Reduction of Bismuth Oxide Nanoparticles and Their Application as an Environmental Sensor. *J Ceram Process Res* **2009**, *10* (2), 190-194.
(70) Chen, X. B.; Liu, L.; Yu, P. Y.; Mao, S. S. Increasing Solar Absorption for Photocatalysis with Black Hydrogenated Titanium Dioxide Nanocrystals. *Science* **2011**, *331* (6018), 746-750. DOI: 10.1126/science.1200448.
(71) Tian, M. K.; Liu, C. Z.; Ge, J. X.; Geohegan, D.; Duscher, G.; Eres, G. Recent Progress in Characterization of the Core-Shell Structure of Black Titania. *J Mater Res* **2019**, *34* (7), 1138-1153. DOI: 10.1557/jmr.2019.46.